

# Terahertz Nanoscopy of Plasmonic Resonances with a Quantum Cascade Laser

Riccardo Degl'Innocenti,<sup>\*,†,‡,⊥</sup> Robert Wallis,<sup>†,⊥</sup> Binbin Wei,<sup>†</sup> Long Xiao,<sup>†,‡</sup> Stephen J. Kindness,<sup>†</sup> Oleg Mitrofanov,<sup>§</sup> Philipp Braeuninger-Weimer,<sup>‡,⊥</sup> Stephan Hofmann,<sup>‡,⊥</sup> Harvey E. Beere,<sup>†</sup> and David A. Ritchie<sup>†</sup>

<sup>†</sup>Cavendish Laboratory, University of Cambridge, J. J. Thomson Avenue, CB3 0HE Cambridge, United Kingdom

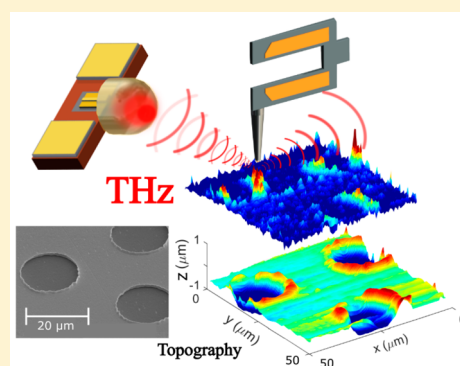
<sup>‡</sup>Department of Engineering, University of Cambridge, J. J. Thomson Avenue, CB3 0FA Cambridge, United Kingdom

<sup>§</sup>Department of Electronic and Electrical Engineering, University College London, Torrington Place, WC1E 7JE London, United Kingdom

## Supporting Information

**ABSTRACT:** We present a terahertz (THz) scattering near-field optical microscope (s-SNOM) based on a quantum cascade laser implemented as both source and detector in a self-mixing scheme utilizing resonant quartz tuning forks as a sensitive nanopositioning element. The homemade s-SNOM, based on a resonant tuning fork and metallic tip, operates in tapping mode with a spatial resolution of  $\sim 78$  nm. The quantum cascade laser is realized from a bound-to-continuum active region design with a central emission of  $\sim 2.85$  THz, which has been lens-coupled in order to maximize the feedback into the laser cavity. Accordingly, the spatial resolution corresponds to  $> \lambda/1000$ . The s-SNOM has been used to investigate a bidimensional plasmonic photonic crystal and to observe the optical resonant modes supported by coupled plasmonic planar antennas, showing remarkable agreement with the theoretical predictions. The compactness, unique sensitivity, and fast acquisition capability of this approach make the proposed s-SNOM a unique tool for solid-state investigations and biomedical imaging.

**KEYWORDS:** near-field microscopy, terahertz, plasmonics, photonic crystals, quantum cascade laser, self-mixing detection



The terahertz (THz) frequency range, 0.1–10 THz, lies in the millimeter and sub-millimeter wavelength range of the electromagnetic spectrum and represents a fast-evolving research area. The increasing efforts in THz science and technology are driven by many fields where such radiation finds applications, mainly in communications, spectroscopy, and imaging.<sup>1,2</sup> In particular, THz imaging is appealing in several areas. In the biomedical research field this nonionizing radiation has been used for diagnostics, due to its capability of discriminating between healthy and cancerous tissues.<sup>3</sup> Near-field imaging techniques have great potential in many applications, ranging from the investigation of the optical properties of solid-state and two-dimensional materials<sup>4–6</sup> to the excitation and direct retrieval of plasmonic resonant modes.<sup>8–11</sup> In semiconductor physics, THz radiation has proved to be a viable tool for inspection of integrated devices with subwavelength resolution.<sup>7</sup> It is well known that THz radiation is sensitive to the doping level of semiconductor devices. Accordingly, it can be implemented for the inspection and mapping of quantum objects even when covered by a dielectric layer, as an alternative and/or complementary technique to photoluminescence techniques. The most commonly used scattering near-field systems are based on

modified atomic force microscopes or commercially available instruments and have proved themselves as efficient tools for the direct mapping and excitation of resonant plasmonic modes in the mid-infrared spectral range.<sup>8–10</sup> Bidimensional materials such as topological insulators<sup>12</sup> or graphene<sup>13</sup> are known to also support surface plasmons in the THz range. Graphene has also been proposed as the basic building block of integrated circuitry.<sup>14</sup> However, the direct excitation of surface plasmons is hindered by the wavevector mismatch between the incoming radiation and the supported modes and typically requires direct patterning or prism-coupling schemes. Near-field microscope probes directly interact with the surface of the object of study through evanescent waves, thus naturally overcoming the dispersion difference. Near-field microscopy thus provides a valuable tool for the excitation of all-plasmonic or hybrid devices. The design of future THz integrated optoelectronic devices, such as amplitude,<sup>15–17</sup> frequency,<sup>18</sup> and polarization<sup>19</sup> modulators, or detectors,<sup>20–22</sup> based on metamaterial/plasmonic subwavelength resonances, relies on the detailed analysis of the properties of a single unit, rather than on ensemble

Received: June 28, 2017

Published: August 28, 2017

averages, thus enforcing the need for a subwavelength inspection tool. Near-field microscopes operating in the THz normally implement cumbersome and unstable gas lasers as sources, such as a CH<sub>3</sub>OH laser pumped by a CO<sub>2</sub> laser.<sup>7,11</sup> Quantum cascade lasers (QCLs)<sup>23</sup> are a more compact, stable, and versatile source to be used in these arrangements. The use of QCLs in aperture<sup>24,25</sup> and apertureless<sup>26</sup> scanning near-field optical microscopes has already been reported with a resolution of  $>1 \mu\text{m}$  as a proof of principle, without an efficient tip/surface feedback system. The self-mixing scheme represents an elegant and powerful approach to THz detection.<sup>27–29</sup> Instead of using slow-responding and/or cryogenic devices such as pyroelectric or Si-bolometer for detection, self-mixing is based on the perturbation introduced by the radiation scattered into the laser cavity by the tip/surface system. By monitoring the change in bias applied to the QCL or the QCL power, it is possible to retrieve information about the amplitude and phase of the scattered electric field. This approach presents many advantages over conventional techniques. It allows a more compact scheme by eliminating the need for extra components. It is an extremely sensitive detection scheme that has been reported to be sensitive to nW power levels,<sup>27</sup> thus making it extremely suitable for the detection of intrinsically weak, omnidirectional scattered signals. Finally, it is a fast detection scheme,<sup>29</sup> since the ultimate limit is given by the QCL dynamics, which typically take place on time scales of picoseconds. Quartz resonant tuning forks (QTFs) have been implemented in near-field microscopy as an alternative to the atomic force microscope cantilevers.<sup>30–32</sup> The resonances supported by these economic and compact elements are based on the piezoelectric effect. Accordingly, a mechanical modification of the resonance amplitude, frequency, or phase translates into a current/voltage change, which then provides the feedback mechanism. Because of their high *Q*-factor and superior stiffness compared to cantilevers, the QTFs are implemented together with sharp metallic tips as an efficient sensitive element in near-field microscopy for the achievement of a constant distance between tip and surface. Their simple circuitry and the lack of an optical illumination feedback system, as required by the cantilever approach, make them the most favorable choice in cryogenic environments<sup>33,34</sup> or in imaging systems susceptible to being optically perturbed.

## RESULTS AND DISCUSSION

Here, we report a THz scattering near-field optical microscope (s-SNOM) system with a resolution of  $\sim 78 \text{ nm}$ , based on a self-mixing detection scheme and implementing QCLs emitting around 2.85 THz as the source/detector. This homemade system has been used to investigate the plasmonic resonances supported by a bidimensional photonic crystal triangular hole array<sup>35</sup> and the electric field enhancement supported in the gap of a graphene/plasmonic antenna THz detector.<sup>21</sup>

The QCL fabrication and coupling to a silicon lens is described in the [Methods](#) section. A schematic of the experimental setup is shown in [Figure 1a](#). The laser light is collimated and focused by two 2 in. *f*/1 off-axis parabolic mirrors with  $\sim 30^\circ$  incident angle. When the beam is illuminating the metallic tip, a positive change in the laser power is detected. The apparatus is then arranged for the collection of the scattered light. The self-mixing scheme used for the acquisition of the THz scattered light is reported in [Figure 1b](#). To amplify the small voltage perturbation on the laser bias  $V_{\text{QCL}}$  caused by the scattered light  $V_{\text{scatt}}$ , it is first

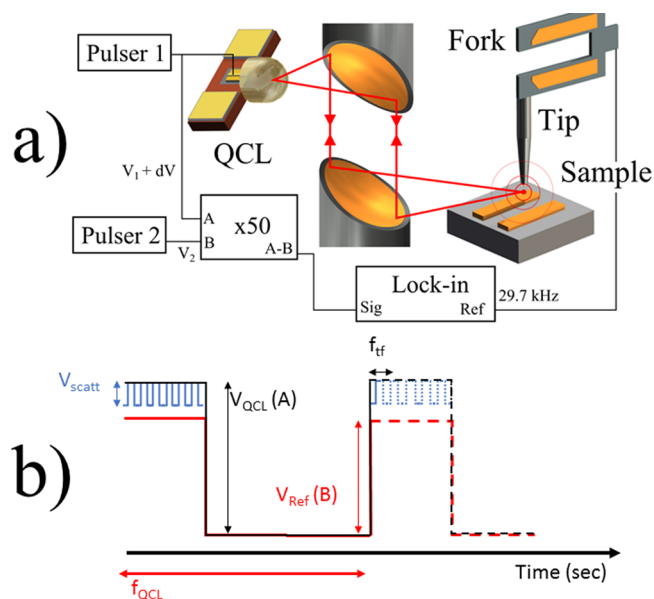


**Figure 1.** (a) Schematic of the apparatus setup. The tuning fork oscillation frequency was set as the reference frequency of the lock-in amplifier. The tip/tuning fork system is arranged in order to operate in tapping mode. The input of the lock-in amplifier was given by the amplified voltage difference between the bias applied to the QCL and another, frequency-synchronized, pulser. (b) Acquisition scheme with the self-mixing technique. The scattered light into the cavity yields a reduction in the bias applied to the QCL,  $V_{\text{QCL}}$ , oscillating at the reference frequency of the tuning fork,  $V_{\text{ref}}$ . This is compared to the bias of a second pulser,  $V_{\text{ref}}$ , before being amplified.

mixed with the bias of an identical pulser  $V_{\text{ref}}$  synchronized to the repetition rate of the QCL  $f_{\text{QCL}}$ , kept fixed to 2 kHz. The voltage difference between the two pulsers  $V_1$  and  $V_2$  in [Figure 1a](#) was kept as low as possible in order to use the minimum sensitivity scale on the lock-in amplifier, thus minimizing the noise. The voltage difference has been magnified in [Figure 1b](#) for clarity. The difference in voltage is then amplified and fed to the lock-in amplifier, which has the resonant frequency of the tuning fork  $f_{\text{tf}}$  as reference. The tuning forks used had a typical resonant frequency of  $\sim 30 \text{ kHz}$ . A higher feedback in the laser cavity corresponds to a reduced bias measured on the QCL, as schematically shown in [Figure 1b](#) and experimentally presented in [Figure S1](#). A metallic tip with a radius of  $<50 \text{ nm}$  is mounted in tapping mode configuration. Further details on the setup and the data acquisition procedure are reported in the [Methods](#) section. A typical measurement example is shown in [Figure 2](#). This picture reports (a) the topography, (b) the THz scattered image, and (c) the optical micrograph of the sample, which consisted of metallic features over a SiO<sub>2</sub> substrate. The sample has two overlapping metallic areas: a vertical stripe achieved with optical lithography (Ti/Au, nominal thickness 10/500 nm) and a horizontal stripe achieved with electron beam lithography (Ti/Au nominal thickness 80/20 nm). According to the standard scattering theory, as presented in refs 36–38, the tip–surface system is modeled as a spherical particle above a planar surface. The incident light induces a dipole in the tip, which is mirrored into the substrate, and the combined dipole system irradiates with an effective polarizability  $\alpha_{\text{eff}}$  given by eq 1:

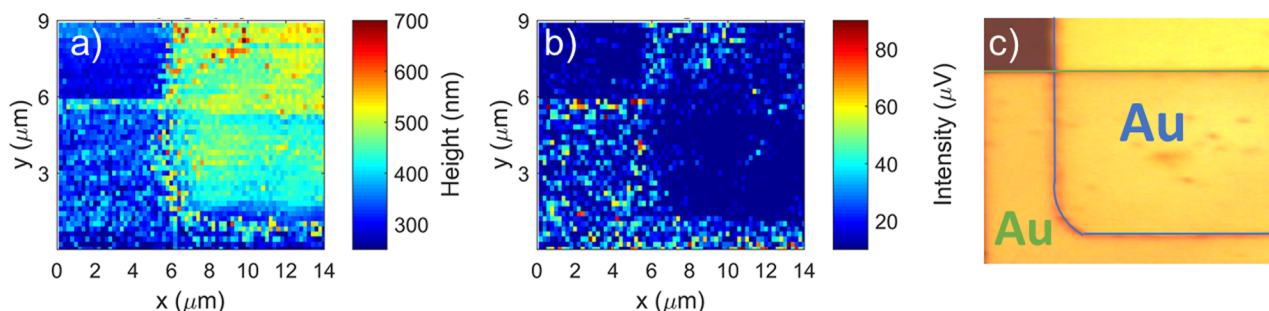


**Figure 2.** Topography (a) and THz image (b) of metallic features on a SiO<sub>2</sub> substrate acquired with a step size of 200 nm. (c) Optical micrograph of the region of interest showing the overlap between two metallic evaporations, over a SiO<sub>2</sub> substrate (top left corner). The metallic region defined with optical lithography (Ti/Au 10/500 nm) is reported in blue. The metallic area fabricated with electron beam lithography (Ti/Au, 80/20 nm) is indicated in green.

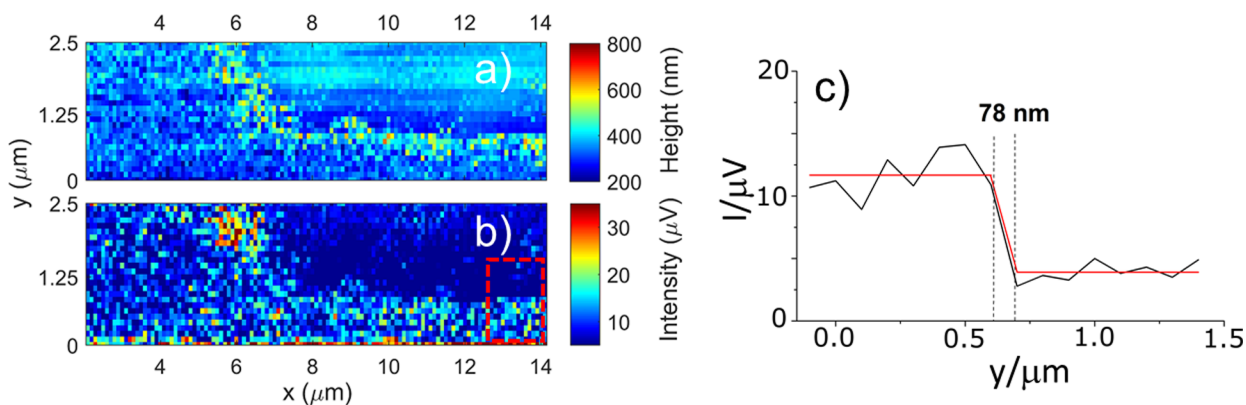


**Figure 3.** Topography (a) and THz image (b) acquired with a 100 nm step size of the metallic features shown in Figure 2. From the profiles extracted in the dashed area in (b) it was possible to obtain an estimation of the spatial resolution of the system (c), calculated to be 78 nm, corresponding to  $>\lambda/1000$ .

$$\alpha_{\text{eff}} = \frac{\alpha(1 + \beta)}{1 - \left(\frac{\alpha\beta}{16\pi(a+z)^3}\right)} \quad (1)$$

where  $\alpha = 4\pi a^3(\epsilon_{\text{tip}} - 1)/(\epsilon_{\text{tip}} + 2)$ ,  $\beta = (\epsilon_{\text{sub}} - 1)/(\epsilon_{\text{sub}} + 1)$ ,  $a$  is the radius of the tip's apex,  $z$  is the relative distance between sample and substrate, and  $\epsilon_{\text{tip}}$  and  $\epsilon_{\text{sub}}$  are the dielectric constant of the tip and substrate, respectively. Assuming a value for the real part of the dielectric constant  $\epsilon_{\text{sub}}$  of 3.9 for the SiO<sub>2</sub> and  $-10\,000$ <sup>39,40</sup> for the Au features and an  $\epsilon_{\text{tip}}$  of  $-40\,000$ <sup>41</sup> for the W-tip having an apex radius of  $\sim 30$  nm, the model predicts a reduced polarizability, hence scattering efficiency, for a dielectric substrate with respect to a metallic one. The THz image presented in Figure 2b shows comparable values for the scattering signals on the SiO<sub>2</sub> and the thicker Au evaporation. According to the polarizability values calculated using eq 1 and reported in Figure S2 in the SI, the ratio between the polarizability, and hence the scattering, yielded by the two different surfaces is  $\sim 1.3$ . The THz signal recorded over the metallic evaporation obtained via e-beam lithography, corresponding to the horizontal stripe, presents a significantly increased signal in comparison with the thick metal evaporation area and the SiO<sub>2</sub> area. This is attributed to the increased roughness, as also shown by the topography, and uniformity of this area. The induced dipole itself and the tip radius have sizes comparable to the roughness and to the total thickness of this metallic layer, which might interact efficiently with the total scattering.

A second scan over the bottom area of Figure 2 has been recorded with a 100 nm step size, and the topography and corresponding THz signal are reported in Figure 3a and b, respectively. Several profiles have been extracted from the dashed area of Figure 3b, to measure the resolution, which, as shown in Figure 3c, was calculated to be  $\sim 78$  nm, by using the 10–90% criterion. This corresponds to a spatial resolution of  $\sim \lambda/1200$ , which is comparable to the resolution achieved at these frequencies with a methanol gas laser,<sup>7</sup> but obtained with an emitting source with  $< \text{mW}$  emitting power and without the need of an extra detecting element. At the same time, this system yielded an improvement of more than 10 times compared to similar near-field systems implementing THz QCLs.<sup>24,25</sup>

The THz s-SNOM system was then used for mapping the plasmonic resonances supported by resonant metallic features. A surface-emitting photonic crystal (SEPHC) QCL<sup>35</sup> based on triangular arrays of holes and emitting around 2.85 THz was chosen since its emission overlapped well with the s-SNOM frequency. The interest in this sample, which was used as a passive element at room temperature, stems from its patterned metallic top contact area and the relative plasmonic resonances supported. A scanning electron microscope (SEM) micrograph of the top contact of the SEPHC is shown in Figure 4a. The patterned metallic surface of the QCL supports dipole modes, as shown in the normalized  $E$ -field reported in Figure 4b simulated with the Comsol Multiphysics finite element commercial software following a procedure explained in refs 16 and 17. The simulated resonant plasmonic modes supported

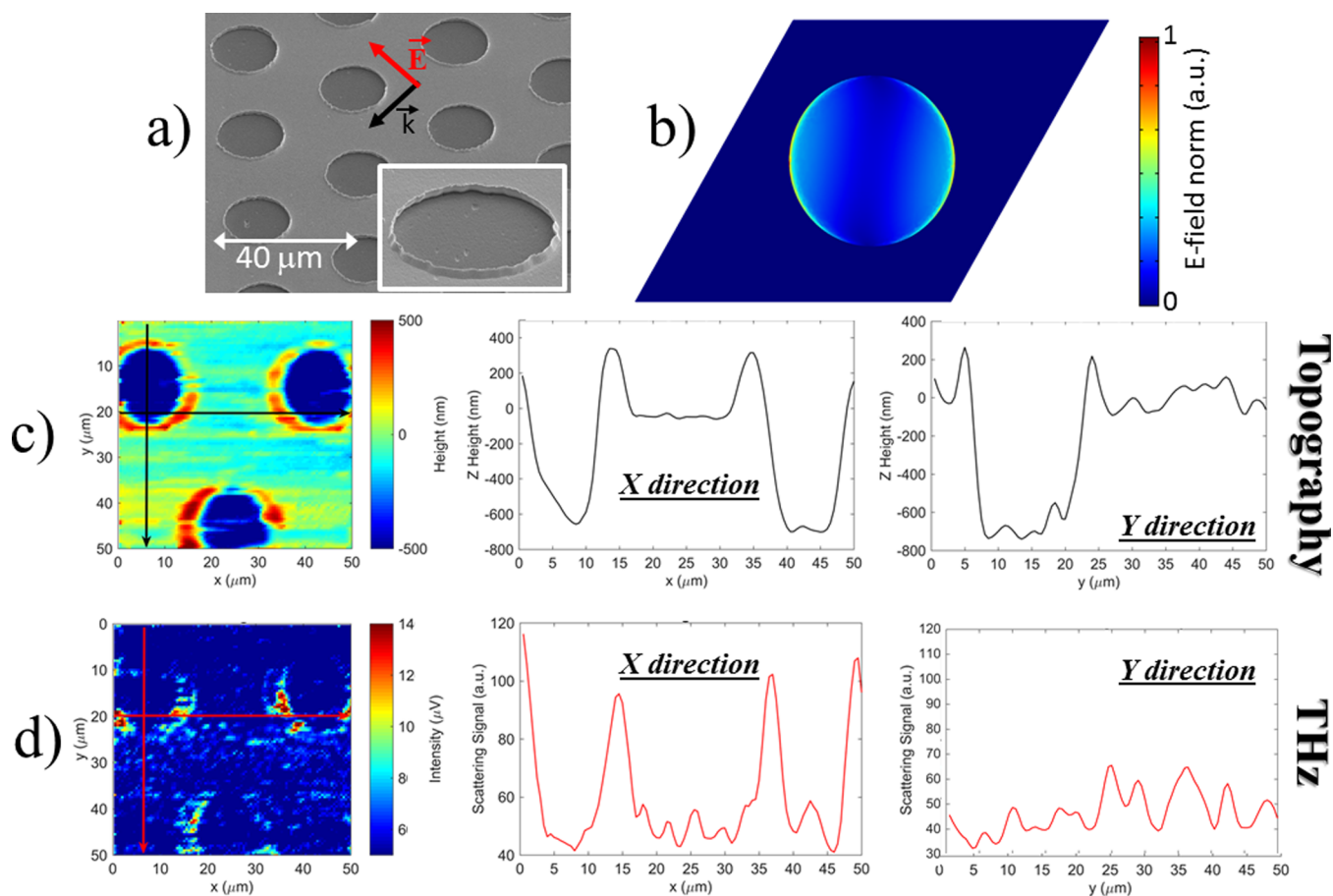


**Figure 4.** Near-field microscopy of an SEPHC QCL emitting around 2.85 THz. (a) SEM micrograph of the QCL top surface patterned with a triangular lattice of holes in a metallic surface for vertical emission. (b) Normalized  $E$ -field at 2.8 THz simulated with Comsol Multiphysics for THz light incident as depicted in (a). (c) Topography and profiles extracted along the two acquisition directions. (d) THz scattered signal and the corresponding profiles extracted.

at 2.8 THz have two distinct peaks along the direction of the incident  $E$ -field. Figure 4c and d report the topography and the retrieved THz scattered signal acquired simultaneously together with the respective profiles extracted along the two corresponding lines. The topography is consistent with the SEM picture and the profiles acquired along the two directions, showing the  $\sim 0.6 \mu\text{m}$  thick metal triangular lattice of holes along the two directions. The image has been smoothed over 3 points, and in some points the tip lost contact with the surface, resulting in missing rows, which have been substituted with the first neighboring points. This operation did not affect the THz signal and also had marginal effects on the topography, as shown by the original data reported in the additional data folder. Because of the lift off the borders of the holes opened on the metallic surface present significant sharp ripples, as shown by the SEM of the inset in Figure 4a and correctly recorded by the topography in Figure 4c. The THz image and the corresponding profiles, shown in Figure 4d, in contrast to the topography, exhibit an asymmetry in the vertical direction with respect to the horizontal one. In particular, two annular peaks are evident along the polarization direction, in good agreement with the simulations presented in Figure 4b. This is consistent with the resonant plasmonic modes supported by the photonic crystal metallic structure. However, due to the sharp metallic rim in the fabrication of the triangular hole array, the THz scattered signal is also strongly influenced by the scanning

direction. This can provide an additional signal, which is likely to be the predominant effect for this specific sample. Because of the irregular metallic border, an increase in the vertical movement of the tip during the scan translates into an increased proximity of the tip and consequently a stronger scattering signal compared to smoother scanning paths, as shown in Figure S2 in the SI.

This uniquely sensitive approach also allows the retrieval of dielectric/plasmonic modes supported in buried resonant structures at these frequencies, such as the one shown in Figure 5. A plasmonic antenna array loaded with graphene was chosen as the object of investigation, similar to the devices already investigated for the bolometric detection of THz QCLs in ref 21 but having a resonant frequency centered around 2.9 THz. The single unit element of the array is composed of planar metallic antennas of size  $15 \times 2 \mu\text{m}^2$ , fabricated on top of a  $\text{SiO}_2/\text{Si}$  substrate and shorted by graphene regions with a  $3 \mu\text{m}^2$  area. All the resonant elements are encapsulated in an  $\text{Al}_2\text{O}_3$  dielectric film up to 100 nm thick deposited by atomic layer deposition. In contrast to the previous device, this presents a smoother metallic border, and the encapsulation with the dielectric layer of  $\text{Al}_2\text{O}_3$  removed the possibility of any other source of extra scattering. The gap between the two antenna arms is  $\sim 300 \text{ nm}$ , as shown by the topography image acquired with the s-SNOM and the extracted profiles of Figure 5a and b, respectively. When the orientation of the incident

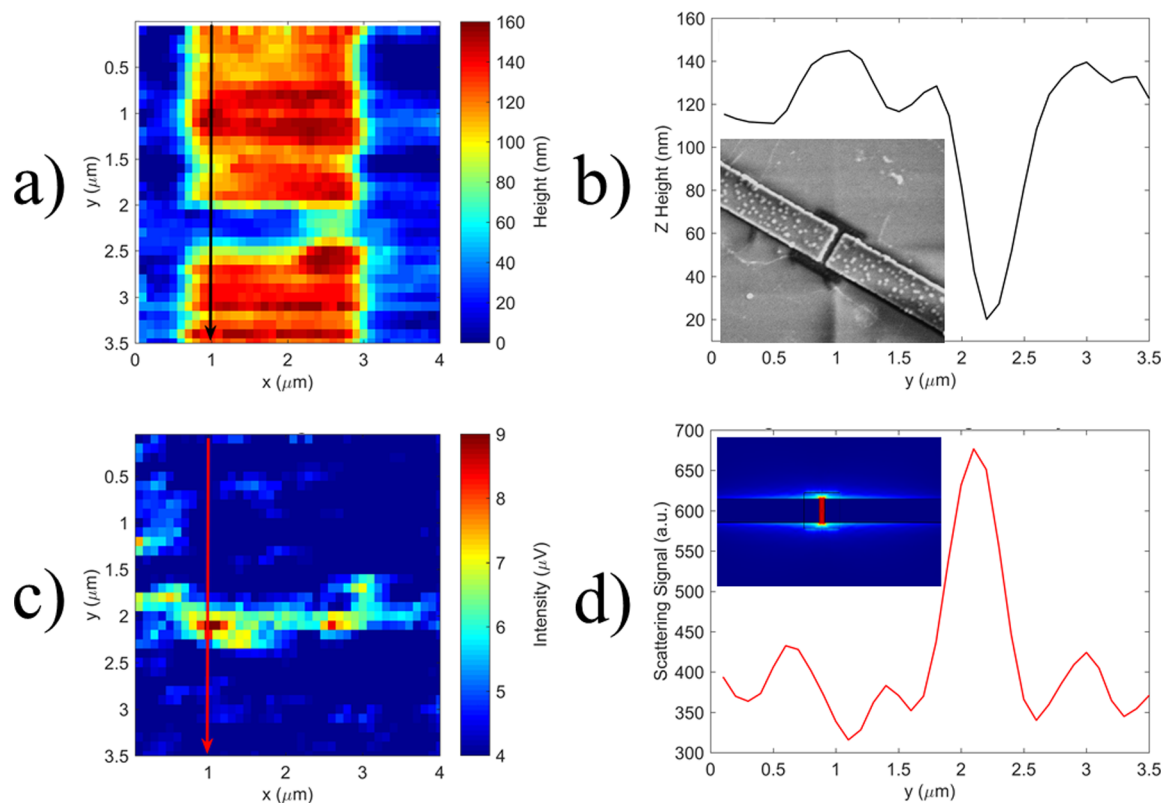


**Figure 5.** Plasmonic resonant antennas loaded with graphene illuminated with the  $E$ -field polarized along the major axis of the antennas. (a) Topography of the resonant elements with a  $\sim 300$  nm gap. (b) Relative extracted profile and SEM micrograph of the same element. (c) THz signal and corresponding profile (d) showing a strong  $E$ -field enhancement in the gap region, in very good agreement with the simulations obtained with the commercial software Comsol Multiphysics and reported in the inset.

polarization was along the main axis of the antennas, the THz topography and the corresponding extracted profile, shown in Figure 5c and d, respectively, presented a strong  $E$ -field enhancement in the gap area. This is in very good agreement with the simulation obtained for the normalized  $E$ -field by using Comsol Multiphysics software and reported in the inset of Figure 5d. Conversely, when the polarization is perpendicular to the main axis of the antenna, a weak THz signal is still observable at the boundary between the metallic antennas and the dielectric, as shown in the SI, but no resonant enhancement of the  $E$ -field is observed in the gap. It seems from the pictures acquired in Figure 4 and Figure 5 that the system is capable of retrieving the enhancement of the  $E$ -field supported by resonant structures. Since the s-SNOM was operating in tapping mode, it should be more sensitive to the vertical component of the  $E$ -field rather than to the in-plane component. According to the simulation performed with Comsol Multiphysics, the two components should have comparable strength. In the case of the resonant antenna of Figure 5, we have not observed a dipolar mode corresponding to the vertical component of the  $E$ -field, but this was attributed to the limited resolution of the system. Operating the s-SNOM in shear-force mode rather than tapping mode might help in determining which component is predominantly retrieved by this system. Demodulation at higher harmonics, which is a common strategy to discriminate the contribution arising from the polarized tip and the illuminated substrate, did not yield a significant improvement in these experiments, but mainly reduced the total collected signal. This effect can be attributed to the limited frequency response of the electronics

implemented for demodulating the signal or to the self-mixing detection scheme itself, which is a strongly nonlinear process based on the amount of scattered photons fed back into the laser cavity.

By further reducing all sources of noise and atmospheric perturbations and placing the whole apparatus in a nitrogen-purged environment, the resolution is expected to improve to  $<30$  nm, a level capable of investigating low-dimensional objects, such as quantum dots or nanowires.<sup>42</sup> The main limits of the current system are represented by the nonoptimal isolation from vibrations and by the environment perturbations. The first issue prevents the system from reaching its full capability in resolution, while the latter is instead responsible for the unwanted fluctuations in the reflected THz signal due to the strong water absorption in the laser path.

This homemade s-SNOM system has advantages over modified atomic force microscopes, in terms of compactness and versatility, thus presenting the possibility of use at cryogenic temperatures. This would facilitate completely new scenarios, allowing the active manipulation of the quantum properties of low-dimensional quantum objects, such as nanowires and quantum dots (QDs). We aim to locally excite QDs or quantum molecules by selectively injecting THz photons in a photon-assisted tunneling experiment where transport is enabled by intraband absorption in the confined hole states of QDs or in the electronic band for molecules. A plethora of new experiments can then be pursued aiming to perform spectroscopy of confined electron–hole systems. Finally, the selective injection of single THz photons could be used to trigger the emission of a single near-infrared photon

from a QD, thus providing a THz-to-telecom bridge in a quantum communication system and leading to the realization of an integrated quantum photon converter. In conclusion, we have demonstrated a THz s-SNOM based on the self-mixing technique using QCLs. A 78 nm resolution, corresponding to  $> \lambda/1000$ , was achieved with a QCL emitting around 2.85 THz. The sensitivity of this approach has been further enhanced by partly suppressing the lasing action and simultaneously increasing the collection efficiency with an antireflection-coated lens attached to a laser facet. The system has been successfully implemented to retrieve the THz image of a photonic crystal lattice of triangular holes and to map the plasmonic modes supported by planar antennas loaded with graphene. This represents significant progress in the field of THz microscopy and paves the way to unique investigations of semiconductor quantum objects, bidimensional materials, and biological samples.

## METHODS

**QCL Fabrication.** The QCL was fabricated with a single plasmon waveguide, with a bound-to-continuum active region emitting around 2.85 THz. In order to enhance the sensitivity of the system, as well as the collection of the scattered light, a silicon lens was attached to the QCL<sup>43</sup> with an 18.5  $\mu\text{m}$  thick antireflection parylene coating. The lens mounting had two primary aims: increasing the collection efficiency of the backscattered light and increasing the cavity mirror loss, rendering the device more similar to a quantum cascade amplifier.<sup>44</sup> By carefully attaching the lens to the facet of the laser using a layer of PMMA (poly(methyl methacrylate)), the emission was strongly reduced but not fully suppressed. A partially suppressed laser emission is needed in order to align the beam onto the metallic tip. The voltage-light-current characteristics of the device with and without feedback are presented in the SI. The laser was operated at the current density corresponding to the maximum emitted power. The optical path was finely adjusted in order to have a maximal backscattered signal into the cavity.

**Acquisition Procedure.** The laser was mounted into the cryostat such that the  $E$ -field had a polarization component along the tip shaft. The tuning fork with the metallic tip was mounted on a printed circuit board connected with a piezoelectric motor stage arranged in the vertical  $z$  direction with 65  $\mu\text{m}$  travel range and 0.13 nm minimum step size. When the system is brought into close proximity to the sample surface, the tuning fork resonance is damped and the frequency, phase, or  $Q$ -factor can be used to close the feedback loop and keep a constant tip/sample distance, typically between 30 and 100 nm. The sample is then scanned in the  $xy$  plane by using two piezoelectric stages with a 250  $\mu\text{m}$  travel range in each direction and 0.4 nm minimum step size. For each  $xy$  position, measurements were recorded for both the height of the tip, yielding the surface topography, and the signal from the lock-in amplifier, corresponding to the THz scattered signal.

## ASSOCIATED CONTENT

### Supporting Information

The Supporting Information is available free of charge on the ACS Publications website at DOI: 10.1021/acsphtonic.7b00687.

Light current–voltage characteristics of the QCL used in this work with and without the feedback; effective

polarizability calculated for different substrates; topography and corresponding THz image of the antenna device shown in the main text but with the incident  $E$ -field polarization perpendicular to the axis of the antenna; relative profiles extracted from the topography and the THz image (PDF)

## AUTHOR INFORMATION

### Corresponding Author

\*E-mail (R. Degl'Innocenti): rd448@cam.ac.uk.

### ORCID

Riccardo Degl'Innocenti: 0000-0003-2655-1997

Philipp Braeuninger-Weimer: 0000-0001-8677-1647

Stephan Hofmann: 0000-0001-6375-1459

### Author Contributions

<sup>†</sup>R. Degl'Innocenti and R. Wallis equally contributed.

### Notes

The authors declare no competing financial interest.

Additional data sets related to this publication are available from the Cambridge University data repository at <https://doi.org/10.17863/CAM.12974>.

## ACKNOWLEDGMENTS

R.D.I., H.E.B., O.M., and D.A.R. acknowledge financial support from the Engineering and Physical Sciences Research Council (Grant No. EP/J017671/1, Coherent Terahertz Systems, and Grant No. EP/P021859/1, HyperTerahertz—High precision terahertz spectroscopy and microscopy). S.H. and P.A.B. acknowledge financial support from the Engineering and Physical Sciences Research Council (Grant No. EP/K016636/1, GRAPHTED).

## REFERENCES

- (1) Dhillon, S. S.; Vitiello, M. S.; Linfield, E. H.; Davies, A. G.; Hoffmann, M. C.; Booske, J.; Paoloni, C.; Gensch, M.; Weightman, P.; Williams, G. P.; Castro-Camus, E.; Cumming, D. R. S.; Simoens, F.; Escorcía-Carranza, I.; Grant, J.; Lucyszyn, S.; Kuwata-Gonokami, M.; Konishi, K.; Koch, M.; Schmittenmaer, C. A.; Cocker, T. L.; Huber, R.; Markelz, A. G.; Taylor, Z. D.; Wallace, V. P.; Axel Zeidler, J.; Sibik, J.; Korter, T. M.; Ellison, B.; Rea, S.; Goldsmith, P.; Cooper, K. B.; Appleby, R.; Pardo, D.; Huggard, P. G.; Krozer, V.; Shams, H.; Fice, M.; Renaud, C.; Seeds, A.; Stöhr, A.; Naftaly, M.; Ridler, N.; Clarke, R.; Cunningham, J. E.; Johnston, M. B. The 2017 terahertz science and technology roadmap. *J. Phys. D: Appl. Phys.* **2017**, *50*, 043001.
- (2) Lee, Y. S. *Principles of Terahertz Science and Technology*; Springer-Verlag: USA, 2009.
- (3) Cheon, H.; Yang, H.-J.; Lee, S.-H.; Kim, Y. A.; Son, J.-H. Terahertz molecular resonance of cancer DNA. *Sci. Rep.* **2016**, *6*, 37103.
- (4) Yazyev, O. V.; Chen, Y. P. Polycrystalline graphene and other two-dimensional materials. *Nat. Nanotechnol.* **2014**, *9*, 755–767.
- (5) Buron, J. D.; Petersen, D. H.; Boeggild, P.; Cooke, D. G.; Hilke, M.; Sun, J.; Whiteway, E.; Nielsen, P. F.; Hansen, O.; Yurgens, A.; Jepsen, P. U. Graphene Conductance Uniformity Mapping. *Nano Lett.* **2012**, *12*, 5074–5081.
- (6) Milot, R. L.; Sutton, R. J.; Eperon, G. E.; Haghghirad, A. A.; Hardigree, J. M.; Miranda, L.; Snaith, H. J.; Johnston, M. B.; Herz, L. M. Charge-Carrier Dynamics in 2D Hybrid Metal–Halide Perovskites. *Nano Lett.* **2016**, *16*, 7001–7007.
- (7) Huber, A. J.; Keilmann, F.; Wittborn, J.; Aizpurua, J.; Hillenbrand, R. Terahertz Near-Field Nanoscopy of Mobile Carriers in Single Semiconductor Nanodevices. *Nano Lett.* **2008**, *8*, 3766–3770.
- (8) Schnell, M.; Sarriurgarte, P.; Neuman, T.; Khanikaev, A. B.; Shvets, G.; Aizpurua, J.; Hillenbrand, R. Real-Space Mapping of the

Chiral Near-Field Distributions in Spiral Antennas and Planar Metasurfaces. *Nano Lett.* **2016**, *16*, 663–670.

(9) Chen, J.; Badioli, M.; Alonso-Gonzalez, P.; Thongrattanasiri, S.; Huth, F.; Osmond, J.; Spasenovic, M.; Centeno, A.; Pesquera, A.; Godignon, P.; Zurutuza Elorza, A.; Camara, N.; Garcia de Abajo, F. J.; Hillenbrand, R.; Koppens, F. H. L. Optical nano-imaging of gate-tunable graphene plasmons. *Nature* **2012**, *487*, 77–81.

(10) Nikitin, A. Y.; Alonso-Gonzalez, P.; Velez, S.; Mastel, S.; Centeno, A.; Pesquera, A.; Zurutuza, A.; Casanova, F.; Hueso, L. E.; Koppens, F. H. L.; Hillenbrand, R. Real-space mapping of tailored sheet and edge plasmons in graphene nanoresonators. *Nat. Photonics* **2016**, *10*, 239–244.

(11) Alonso-Gonzalez, P.; Nikitin, A. Y.; Gao, Y.; Woessner, A.; Lundberg, M. B.; Principi, A.; Forcellini, N.; Yan, W.; Velez, S.; Huber, A. J.; Watanabe, K.; Taniguchi, T.; Casanova, F.; Hueso, L. E.; Polini, M.; Hone, J.; Koppens, F. H. L.; Hillenbrand, R. Acoustic terahertz graphene plasmons revealed by photocurrent nanoscopy. *Nat. Nanotechnol.* **2017**, *12*, 31–35.

(12) Di Pietro, P.; Ortolani, M.; Limaj, O.; Di Gaspare, A.; Giliberti, V.; Giorgianni, F.; Brahlek, M.; Bansali, N.; Koirala, N.; Oh, S.; Calvani, P.; Lupi, S. Observation of Dirac plasmons in a topological insulator. *Nat. Nanotechnol.* **2013**, *8*, 556–560.

(13) Ju, L.; Geng, B.; Horng, J.; Girit, C.; Martin, M.; Hao, Z.; Bechtel, H. A.; Lian, X.; Zettl, A.; Ron Shen, Y.; Wang, F. Graphene plasmonics for tunable terahertz metamaterials. *Nat. Nanotechnol.* **2011**, *6*, 630–634.

(14) Vakil, A.; Engheta, N. Transformation Optics Using Graphene. *Science* **2011**, *332*, 1291–1294.

(15) Jadidi, M. M.; Sushkov, A. B.; Myers-Ward, R. L.; Boyd, A. K.; Daniels, K. M.; Gaskill, D. K.; Fuhrer, M. S.; Drew, H. D.; Murphy, T. E. Tunable Terahertz Hybrid Metal–Graphene Plasmons. *Nano Lett.* **2015**, *15*, 7099–7104.

(16) Jessop, D. S.; Kindness, S. J.; Xiao, L.; Braeuninger-Weimer, P.; Lin, H.; Ren, Y.; Ren, C. X.; Hofmann, S.; Zeitler, J. A.; Beere, H. E.; Ritchie, D. A.; Degl'Innocenti, R. Graphene based plasmonic terahertz amplitude modulator operating above 100 MHz. *Appl. Phys. Lett.* **2016**, *108*, 171101.

(17) Degl'Innocenti, R.; Jessop, D. S.; Sol, C. W. O.; Xiao, L.; Kindness, S. J.; Lin, H.; Zeitler, J. A.; Braeuninger-Weimer, P.; Hofmann, S.; Ren, Y.; Kamboj, V. S.; Griffiths, J.; Beere, H. E.; Ritchie, D. A. Fast Modulation of Terahertz Quantum Cascade Lasers Using Graphene Loaded Plasmonic Antennas. *ACS Photonics* **2016**, *3*, 464–470.

(18) Chen, H.-T.; O'Hara, J. F.; Azad, A. K.; Taylor, A. J.; Averitt, R. D.; Shrekenhamer, D. B.; Padilla, W. J. Experimental demonstration of frequency-agile terahertz metamaterials. *Nat. Photonics* **2008**, *2*, 295–298.

(19) Zhou, J.; Chowdhury, D. R.; Zhao, R.; Azad, A. K.; Chen, H.-T.; Soukoulis, C. M.; Taylor, A. J.; O'Hara, J. F. Terahertz chiral metamaterials with giant and dynamically tunable optical activity. *Phys. Rev. B: Condens. Matter Mater. Phys.* **2012**, *86*, 035448.

(20) Cai, X.; Sushkov, A. B.; Suess, R. J.; Jadidi, M. M.; Jenkins, G. S.; Nyakiti, L. O.; Myers-Ward, R. L.; Li, S.; Yan, J.; Gaskill, D. K.; Murphy, T. E.; Drew, H. D.; Fuhrer, M. S. Sensitive room-temperature terahertz detection via the photothermoelectric effect in graphene. *Nat. Nanotechnol.* **2014**, *9*, 814–819.

(21) Degl'Innocenti, R.; Xiao, L.; Kindness, S. J.; Kamboj, V.; Wei, B.; Braeuninger-Weimer, P.; Nakanishi, K.; Aria, A.; Hofmann, S.; Beere, H. E.; Ritchie, D. A. Bolometric detection of terahertz quantum cascade laser radiation with graphene-plasmonic antenna arrays. *J. Phys. D: Appl. Phys.* **2017**, *50*, 174001.

(22) Degl'Innocenti, R.; Xiao, L.; Jessop, D. S.; Kindness, S. J.; Ren, Y.; Lin, H.; Zeitler, J. A.; Alexander-Webber, J. A.; Joyce, H. J.; Braeuninger-Weimer, P.; Hofmann, S.; Beere, H. E.; Ritchie, D. A. Fast Room-Temperature Detection of Terahertz Quantum Cascade Lasers with Graphene-Loaded Bow-Tie Plasmonic Antenna Arrays. *ACS Photonics* **2016**, *3*, 1747–1753.

(23) Williams, B. Terahertz quantum-cascade lasers. *Nat. Photonics* **2007**, *1*, 517–525.

(24) Degl'Innocenti, R.; Montinaro, M.; Xu, J.; Piazza, V.; Pingue, P.; Tredicucci, A.; Beltram, F.; Beere, H. E.; Ritchie, D. A. Differential near-field scanning optical microscopy with THz quantum cascade laser sources. *Opt. Express* **2009**, *26*, 23785–23792.

(25) Mitrofanov, O.; Viti, L.; Dardanis, E.; Caterina Giordano, M.; Ercolani, D.; Politano, A.; Sorba, L.; Vitiello, M. S. Near-field terahertz probes with room-temperature nanodetectors for subwavelength resolution imaging. *Sci. Rep.* **2017**, *7*, 44240.

(26) Dean, P.; Mitrofanov, O.; Keeley, J.; Kundu, I.; Li, L.; Linfield, E. H.; Davies, A. G. Apertureless near-field terahertz imaging using the self-mixing effect in a quantum cascade laser. *Appl. Phys. Lett.* **2016**, *108*, 091113.

(27) Dean, P.; Lim, Y. L.; Valavanis, A.; Kliese, R.; Nikolić, M.; Khanna, S. P.; Lachab, M.; Indjin, D.; Ikončić, Z.; Harrison, P.; Rakić, A. D.; Linfield, E. H.; Davies, A. G. Terahertz imaging through self-mixing in a quantum cascade laser. *Opt. Lett.* **2011**, *36*, 2587–2589.

(28) Valavanis, A.; Dean, P.; Lim, Y. L.; Alhathlool, R.; Nikolic, M.; Kliese, R.; Khanna, S. P.; Indjin, D.; Wilson, S. J.; Rakić, A. D.; Linfield, E. H.; Davies, A. G. Self-Mixing Interferometry With Terahertz Quantum Cascade Lasers. *IEEE Sens. J.* **2013**, *13*, 37–43.

(29) Ren, Y.; Wallis, R.; Jessop, D. S.; Degl'Innocenti, R.; Klimont, A.; Beere, H. E.; Ritchie, D. A. Fast terahertz imaging using a quantum cascade amplifier. *Appl. Phys. Lett.* **2015**, *107*, 011107.

(30) Karrai, K.; Grober, R. Piezoelectric tip-sample distance control for near field optical microscopes. *Appl. Phys. Lett.* **1995**, *66*, 1842–1844.

(31) Ruitter, A. G.; Veerman, J. A.; Van Der Werf, K. O.; Van Hulst, N. F. Dynamic behavior of tuning fork shear-force feedback. *Appl. Phys. Lett.* **1997**, *71*, 28–30.

(32) Atia, W. A.; Davis, C. C. A Phase-Locked Shear-Force Microscope for Distance Regulation in Near-Field Optical Microscopy. *Appl. Phys. Lett.* **1997**, *70*, 405–407.

(33) Rychen, J.; Ihn, T.; Studerus, P.; Herrmann, A.; Ensslin, K. A low-temperature dynamic mode scanning force microscope operating in high magnetic fields. *Rev. Sci. Instrum.* **1999**, *70*, 2765–2768.

(34) Yang, C. H.; Chang, T. H.; Yang, M. J.; Moore, W. J. A low noise transimpedance amplifier for cryogenically cooled quartz tuning fork force sensors. *Rev. Sci. Instrum.* **2002**, *73*, 2713–2716.

(35) Marshall, O. P.; Apostolopoulos, V.; Freeman, J. R.; Rungsawang, R.; Beere, H. E.; Ritchie, D. A. Surface-emitting photonic crystal terahertz quantum cascade lasers. *Appl. Phys. Lett.* **2008**, *93*, 171112.

(36) Novotny, L.; Hecht, B. *Principle of Nano-Optics*, 3rd ed.; Cambridge University Press: Cambridge, UK, 2007.

(37) Knoll, B.; Keilmann, F. Near-field probing of vibrational absorption for chemical microscopy. *Nature* **1999**, *399*, 134–137.

(38) Knoll, B.; Keilmann, F. Enhanced dielectric contrast in scattering-type scanning near-field microscopy. *Opt. Commun.* **2000**, *182*, 321–328.

(39) Ordal, M. A.; Long, L. L.; Bell, R. J.; Bell, S. E.; Bell, R. R.; Alexander, R. W., Jr; Ward, C. A. Optical properties of the metals Al, Co, Cu, Au, Fe, Pb, Ni, Pd, Pt, Ag, Ti, and W in the infrared and far infrared. *Appl. Opt.* **1983**, *22*, 1099–1120.

(40) Ordal, M. A.; Bell, R. J.; Alexander, R. W.; Long, L. L.; Querry, M. R. Optical properties of fourteen metals in the infrared and far infrared: Al, Co, Cu, Au, Fe, Pb, Mo, Ni, Pd, Pt, Ag, Ti, V, and W. *Appl. Opt.* **1985**, *24*, 4493–4499.

(41) Ordal, M. A.; Bell, R. J.; Alexander, R. W.; Newquist, L. A.; Querry, M. R. Optical properties of Al, Fe, Ti, Ta, W, and Mo at submillimeter wavelengths. *Appl. Opt.* **1988**, *27*, 1203–1209.

(42) Eisele, M.; Cocker, T. L.; Huber, M. A.; Plankl, M.; Viti, L.; Ercolani, D.; Sorba, L.; Vitiello, M. S.; Huber, R. Ultrafast multi-terahertz nano-spectroscopy with sub-cycle temporal resolution. *Nat. Photonics* **2014**, *8*, 841–845.

(43) Degl'Innocenti, R.; Shah, Y. D.; Jessop, D. S.; Ren, Y.; Mitrofanov, O.; Beere, H. E.; Ritchie, D. A. Hollow metallic waveguides integrated with terahertz quantum cascade lasers. *Opt. Express* **2014**, *22*, 24439–24449.

(44) Ren, Y.; Wallis, R.; Shah, Y. D.; Jessop, D. S.; Degl'Innocenti, R.; Klimont, A.; Kamboj, V.; Beere, H. E.; Ritchie, D. A. Single mode terahertz quantum cascade amplifier. *Appl. Phys. Lett.* **2014**, *105*, 141102.